



HAL
open science

SPICE Modeling in Verilog-A for Photo-Response in UTC-Photodiodes Targeting Beyond-5G Circuit Design

Mukherjee Chhandak, D. Guendouz, M. Deng, H. Bertin, A. Bobin, N. Vaissiere, C. Caillaud, A. Arabhavi, R. Chaudhary, O. Ostinelli, et al.

► **To cite this version:**

Mukherjee Chhandak, D. Guendouz, M. Deng, H. Bertin, A. Bobin, et al.. SPICE Modeling in Verilog-A for Photo-Response in UTC-Photodiodes Targeting Beyond-5G Circuit Design. IEEE Transactions on Computer-Aided Design of Integrated Circuits and Systems, 2023, 42 (9), pp.3045-3052. 10.1109/TCAD.2023.3236277 . hal-04230873

HAL Id: hal-04230873

<https://hal.science/hal-04230873>

Submitted on 6 Oct 2023

HAL is a multi-disciplinary open access archive for the deposit and dissemination of scientific research documents, whether they are published or not. The documents may come from teaching and research institutions in France or abroad, or from public or private research centers.

L'archive ouverte pluridisciplinaire **HAL**, est destinée au dépôt et à la diffusion de documents scientifiques de niveau recherche, publiés ou non, émanant des établissements d'enseignement et de recherche français ou étrangers, des laboratoires publics ou privés.

SPICE Modeling in Verilog-A for Photo-response in UTC-photodiodes targeting Beyond-5G Circuit Design

C. Mukherjee, *Member, IEEE*, D. Guendouz, M. Deng, *Member, IEEE*, H. Bertin, A. Bobin, N. Vaissiere, C. Caillaud, A. M. Arabhavi, R. Chaudhary, O. Ostinelli, C. Bolognesi, *Fellow, IEEE*, P. Mounaix, and C. Maneux, *Member, IEEE*

Abstract— This paper reports the first accurate and physics-based Verilog-A implementation of the fully analytic form of photocurrent in SPICE compact models for uni-traveling carrier (UTC) photodiodes (PD). To overcome the limitations of single pole network implementations for modeling frequency dependence of the photo-response, especially at frequencies beyond 100 GHz, we explored different solutions for the complete analytic equation of the dynamic photocurrent. A new implementation has been proposed which requires three additional nodes in the UTC-PD electrical equivalent circuit and offers the best trade-off between accuracy and computational efficiency. Model validation has been performed against on-wafer measurements from two UTC-PD technologies depicting very good accuracy over the entire frequency range.

Index Terms— Beyond-5G circuit design, Photodiode compact model, UTC photodiode, SPICE, Verilog-A.

I. INTRODUCTION

OPTOELECTRONIC integrated circuits (OEIC) are a fast-emerging technology to meet the growing demands of broadband communications especially for beyond-5G networks. These circuits can be realized through efficient technological convergence between electronic and photonic systems, such as monolithic integration on InP substrate [1, 2]. This leverages cost-efficiency of on-chip integration, uni-traveling carrier (UTC) photodiodes (PD) for optical to millimetre-wave conversion [2, 3] and high-speed InP HBTs particularly suited for terahertz applications owing to high electron mobility and breakdown fields [4]. Designing such photonic integrated circuits naturally prompts the need to leverage existing electronic circuit design framework as well as compatible, computationally efficient, and physics-based models for individual devices. From the compatibility viewpoint for circuit design tools, SPICE models are of crucial importance in photonic device modeling. At present, the existing handful of SPICE-compatible modeling efforts [5-9] in photonics, especially for UTC-photodiodes, are largely based on an equivalent circuit modeling approach. While these equivalent circuit models, consisting of R-C equivalent networks, capture the behaviour of UTC-PDs reasonably well and thus offer computational advantage over numerical models, the physical basis of these models remain limited compared to a physics-based and scalable SPICE compact

model in Verilog-A. Moreover, the simplicity of the existing equivalent circuit models limit their accuracy compared to analytic equations describing the physics of UTC-PDs [10-12]. In an effort to bring SPICE models closer to the physical transport mechanisms, a comprehensive SPICE model in Verilog-A, which accounts for both static and dynamic behavior of UTC-PDs, was presented in [13] and further detailed in [14-15]. However, due to the inherent complexity in implementing the analytical equations describing the photo-response in Verilog-A, behavioral approximations were used that limit the model's physical basis as well as its accuracy at higher frequencies. To circumvent this problem, in this work we explore a more accurate, yet computationally optimum, Verilog-A implementation of the photo-response. At frequencies beyond 110 GHz, particularly where photodiode bandwidths can potentially reach several hundreds of GHz [16-17], our proposed implementation remains accurate in comparison with the analytical solution.

The rest of the paper is organized as follows: Section II describes the background of this work detailing the limitations in previous modeling approaches; Section III describes different approximation methods and corresponding model equations for the Verilog-A implementation, followed by a theoretical comparison of the implementations with the full analytical model; Section IV compares the accuracy of different model implementation and details model validation against on-wafer measurements of photo-response on two III-V UTC-PD technologies.

II. BACKGROUND

The electrical equivalent circuit of the UTC-PD [13], illustrated in Fig. 1 (a), consists of two current sources in parallel, the classical diode current, $I_D = I_S[\exp(V_d/nV_T) - 1]$, and the photocurrent, I_{photo} , under reverse bias. The p-n junction capacitance of the diode is denoted by the C_{j0} , in parallel with the reverse bias p-n junction resistance R_{sh} of the fully depleted junction. R_{series} is the resistance of the diode in series with the anode. C_P and L_P are the parasitic capacitance and inductances due to the measured test structures (RF-pads). The photocurrent is controlled by the input optical power and is modelled by the photo-generation rate and the transfer functions in the absorber and collector regions. While the Verilog-A model presented in [13-15], captured both the static and dynamic behavior of UTC-PDs quite well, the dynamic photocurrent modeling remained rather simplified. This is because the implementation of the complete analytical form is not straightforward due to the complex *sinc* and exponential functions representing its frequency dependence. The analytical photocurrent model discussed in this work was originally developed by Ishibashi *et al.* [10], where the

C. Mukherjee, D. Guendouz, M. Deng, P. Mounaix and C. Maneux are with the IMS Laboratory, University of Bordeaux, 351, Cours de la Libération - 33405 Talence, France (e-mail: chhandak.mukherjee@ims-bordeaux.fr).

H. Bertin, A. Bobin, N. Vaissiere and C. Caillaud are with III-V Lab, A Joint Lab between Nokia Bell Labs, Thales Research & Technology and CEA-LETI, 91767 Palaiseau, France (e-mail: christophe.caillaud@3-5lab.fr).

A. M. Arabhavi, R. Chaudhary, O. Ostinelli and C. Bolognesi are with ETH-Zurich, Switzerland (e-mail: bolognesi@mwe.ee.ethz.ch).

photocurrent was calculated for a simple UTC-PD structure with an absorption layer of thickness W_A and a collection layer of thickness W_C . The analytical solution is obtained using the current continuity relation, the drift diffusion equations and the Poisson's equation under the short-circuit condition. In [11], Ishibashi *et al.* developed an improved formulation of the total photocurrent density obtained by following current continuity across the absorber and the collector regions,

$$J_{tot}(\omega) = J_A(\omega) + j \frac{\omega \epsilon_s}{W_A} V_A(\omega) + J_{adj}(\omega) \quad (1)$$

$$= J_C(\omega) + j \frac{\omega \epsilon_s}{W_C} V_C(\omega) \quad (2)$$

Where, $J_A(\omega)$ and $V_A(\omega)$ are the photocurrent and voltage drop in the absorber, respectively. $J_C(\omega)$ and $V_C(\omega)$ are the photocurrent and voltage drop in the collector layer, respectively; ϵ_s is the permittivity of the material. Considering that the electron velocity is constant, and the transfer function $H_C(\omega) = \frac{\sin(\omega\tau_c/2)}{\omega\tau_c/2} e^{-j\frac{\omega\tau_c}{2}}$, for the induced current in the carrier collecting layer [10, 11], then $J_A(\omega)$ [11] and $J_C(\omega)$ [10] are given by:

$$J_A(\omega) = -qG(\omega) \times H_A(\omega) = -qG(\omega) \frac{1}{1 + j\omega\tau_a} \quad (3)$$

$$J_C(\omega) = J_A(\omega) \times H_C(\omega) = -qG(\omega) \frac{1}{1 + j\omega\tau_a} \frac{\sin(\omega\tau_c/2)}{\omega\tau_c/2} e^{-j\frac{\omega\tau_c}{2}} \quad (4)$$

Here, $G(\omega)$ is electron-hole pair generation rate uniformly distributed over the absorber of thickness W_A . As $J_A(\omega)$ and $J_C(\omega)$ differ in amplitude and phase, an additional current term, $J_{adj}(\omega)$ was added in (1) to satisfy the current continuity. For the terminal voltage of the photodiode to be zero under short circuit condition, the following must be satisfied ([11]):

$$j \frac{\omega \epsilon_s}{W_A} V_A(\omega) = -j \frac{\omega \epsilon_s}{W_C} V_C(\omega) \quad (5)$$

At the low frequency limit ($\ll f_{3DB}$), $J_A(\omega)$ equals $J_C(\omega)$. Then the term $J_{adj}(\omega)$ is approximated by:

$$J_{adj}(\omega) = -2j \frac{\omega \epsilon_s}{W_A} V_A(\omega) \quad (6)$$

$$\text{or, } J_{adj}(\omega) \approx -j\omega C_A R_A J_A(\omega) = -j\omega\tau_{adj} J_A(\omega) \quad (7)$$

Where C_A and R_A are absorber capacitance and resistance, respectively. The product $C_A R_A$ is the adjustment time τ_{adj} and it is estimated to be several tens of fs for a p-InGaAs absorber with low resistivity and small thickness [11]. At lower frequencies (< 500 GHz), $\omega\tau_{adj} \ll 1$. Therefore, the collector displacement current $-j \frac{\omega \epsilon_s}{W_C} V_C(\omega)$ can be ignored and from (2) the total photocurrent becomes:

$$J_{tot}(\omega) \approx -qG(\omega) \frac{1}{1 + j\omega\tau_a} \frac{\sin(\omega\tau_c/2)}{\omega\tau_c/2} e^{-j\frac{\omega\tau_c}{2}} \quad (8)$$

Assuming that the sinusoidal generation rate $G(\omega)$ is constant throughout the absorption region, W_A , one can rewrite the above as,

$$I_{tot}(\omega) = -I_{ph0} \frac{1}{1 + j\omega\tau_a} \text{sinc}(\omega\tau_c/2) e^{-j\frac{\omega\tau_c}{2}} \quad (9)$$

This expression can also be found in [18].

Considering the static photocurrent of the UTC-PD, $I_{ph}(\omega = 0) = I_{ph0}$, the dynamic photocurrent has been derived as a function of the transit times across the absorber, τ_a , and the collector, τ_c [10], which are given by,

$$\tau_a = \left(\frac{W_A^2}{3D_e} + \frac{W_A}{v_{th}} \right), \quad (10)$$

$$\tau_c = \frac{W_C}{v_c} \quad (11)$$

Here, W_A and W_C are absorber and collector thicknesses, respectively, v_{th} and v_c are thermionic and carrier saturation velocities in the absorber and collector, respectively, and D_e is the electron diffusion coefficient in the absorber, calculated using the mobility through the Einstein relation, $D_e/\mu_e = kT/q$.

The full extent of precision of the analytical expression in (9) could not be validated experimentally, especially due to the difficulty in measuring the phase of the device photo-response correctly as parasitic contributions from the optical measurement setup could not be removed. Hence, we constructed a theoretical InGaAs/InP UTC-PD device that closely resembles our experimental DUTs, using TCAD simulation with SILVACO [19]. In Fig. 1, the simulated mesa structure of the InGaAs/InP UTC-PD is shown depicting different epitaxial layers and their corresponding doping profiles. In the TCAD simulation, we used the same physical parameters as the calculation of the analytical expression of (9), such as the absorber and collector thicknesses of 100 and 225 nm, respectively. From the range of values found in [12] for the mobility, we used an electron mobility of $0.5 \text{ m}^2/\text{Vs}$ for all our calculations that corresponds to the absorption layer doping level in our case. The key parameters used in our simulations are summarized in table 1.

Table 1: Physical parameter values used in eq. (9)

Physical parameters	Value
W_A (nm)	100
W_C (nm)	225
v_{th} (m/s) (InGaAs)	2.5×10^5
v_c (m/s) (InP)	1×10^5
μ_e ($\text{m}^2/\text{V.s}$)	0.5

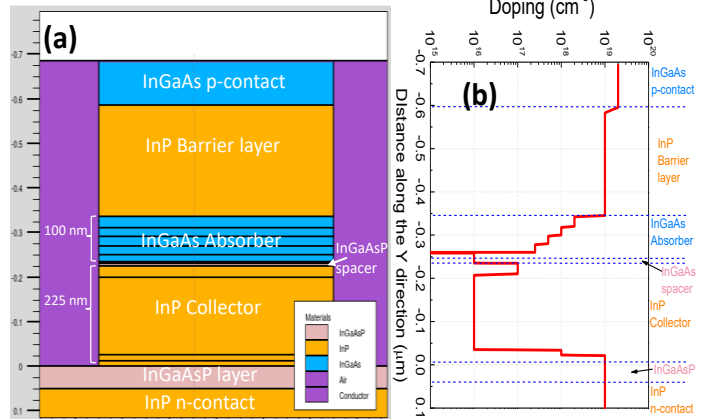


FIG. 1: (a) Epitaxial structure depicting layer compositions and thicknesses of different materials and (b) doping profile of the TCAD simulated UTC-PD.

Next, we performed optical TCAD simulation for which a light beam of $1.55 \mu\text{m}$ wavelength was used to illuminate the device vertically (Fig. 2 (a)) which led to photo-generation of carriers mainly in the InGaAs absorber and p-contact layers (Fig. 2(b)). AC optical simulation was then performed from which we extracted the real and imaginary parts of the photocurrent (Fig. 2(c)), which were then converted to the normalized magnitude and phase of the photo-response as shown in Fig. 2(d) and (e), respectively. While the TCAD simulated device did not include the contributions from the interconnects of extrinsic test-structure of the real device, the

R-C response of the intrinsic diode (due to the series resistance and the p-n junction capacitance) was still present in the simulation, which needed to be accounted for when comparing with the pure theoretical photo-response described by (9) as depicted in Fig. 2(d)-(e). Hence, we used the series resistance and junction capacitance values (Fig. 2) obtained from the TCAD simulation of the unilluminated device. Consequently, the transfer function of the photo-only response in (9) was multiplied by the transfer function of the diode R-C response to obtain a fair comparison with TCAD data. Figs. 2 (c), (d) and (e) show a good agreement between the TCAD and analytical model simulations, affirming the validity of the latter. Moreover, a recent Monte Carlo simulation study by Ishibashi *et al.* [20] has provided further validation of their earlier works on the analytical model such as [11], on which this work is based. For subsequent theoretical analysis presented in the following sections, we have focused on the photo-only analytical expression of (9) for comparison with other theoretical implementations explored in this work.

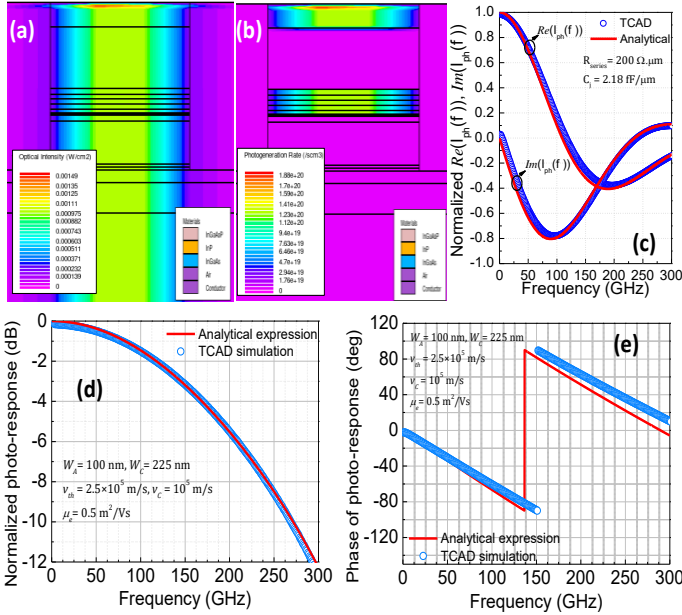


FIG. 2: Optical simulation using SILVACO TCAD depicting (a) optical intensity; (b) photo-generation rate; Normalized photo-response showing (c) real and imaginary parts (d) magnitude and (e) phase in comparison with the analytical model of eq. (9).

Direct frequency-domain implementations of *sinc* and exponential functions in Verilog-A are not possible and therefore no SPICE Verilog-A model exists to-date that takes into account the complete analytical eq. (9). Rudimentarily, the dynamic behavior in (9) can be represented using a low-pass filter like single-pole R-C network to model the frequency roll-off. The additional electrical equivalent circuit uses a unit resistance (in Ω) and a capacitance of value τ_t (in F) in parallel fed by a current source I_{ph0} , thus implementing $I_{ph}(w) = I_{ph0}/(1 + jw\tau_t)$ (inset of Fig. 3(a)). However, this largely overestimates the analytical solution as frequency increases. Moreover, this approximation accounts for only one type of carrier in a unipolar region and thus cannot capture the complete physics of carrier transport in devices like p-i-n diodes or UTC-PDs. Considering absorber and collector thicknesses of 100 and 225 nm, respectively, a v_{th} of 2.5×10^5

m/s as well as a v_c of 10^5 m/s [10] in (9) for an InGaAs/InP UTC-PDs, the magnitude and phase of the normalized frequency response (I_{ph}/I_{ph0}) is plotted in Figs. 3 (b) and (c) for both the analytical equation and the single pole approximation. Note that we have used the value of τ_t to be the same as τ_a in (9) calculated with a mobility of $0.5 \text{ m}^2/\text{Vs}$. Even with a mobility of $0.26 \text{ m}^2/\text{Vs}$ from [11], we observe that the single pole model still largely overestimates both magnitude and phase (Fig. 3). This implementation, thus, does not meet the criteria for design of high-speed optoelectronic circuits using SPICE. Interestingly, only the phase of the photocurrent is governed by the $e^{-j\omega\tau_c/2}$ term in (9) and without this term, the phase of the photocurrent in (9) reduces to that of the single pole implementation (Fig. 3(c)) even though its magnitude remains the same as that of (9). From the point of view of design and understanding of microwave photonic systems, capturing both magnitude and phase of the frequency response of photodiodes is crucial yet remains experimentally difficult as reported previously [21-22]. This in turn, limits the understanding of the operation of the photodiode and as a result the prediction of system level performances [23]. Even though important figures of merit of the photodiode, such as its 3-dB bandwidth and power, are both calculated simply from the magnitude of the photo-response, the phase is important from the perspective of the whole system as it is also dependent on the optical energy. Phase variations often come with excess phase noise and can thus impede demodulation [24]. Hence, it is crucial that the SPICE implementation also captures the phase of the photo-response accurately along with the magnitude of the photocurrent. With that in mind, in this work, we explore more accurate implementation of (9) and develop the first Verilog-A implementation of an accurate and computationally efficient SPICE model for describing the complete analytical photocurrent expression in UTC-PDs. Our proposed implementation methodology is not technology-specific and can be extended for other photonic devices such as high-bandwidth (>200 GHz) p-i-n photodiodes [16].

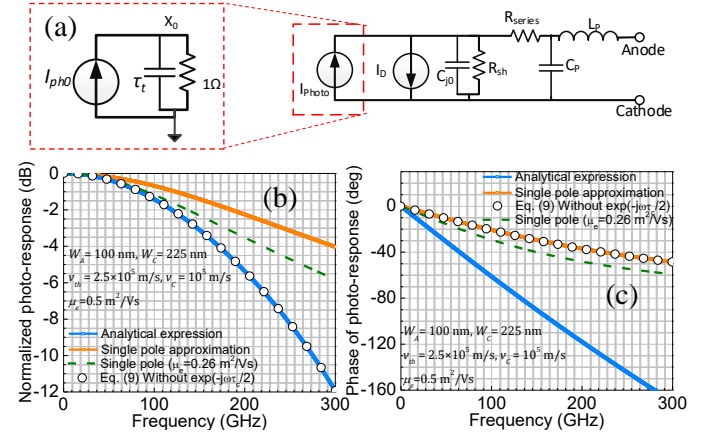


FIG. 3: (a) UTC-PD Electrical equivalent circuit; inset showing photocurrent implementation using an additional node; (b) Normalized frequency response of UTC-PD comparing the analytical and approximate solutions.

III. MODEL EQUATIONS AND VERILOG-A IMPLEMENTATION

The central idea behind this work has been to develop model equations for Verilog-A implementations that capture the dynamic photocurrent behavior in UTC-PDs by approximating eq. (9) as accurately as possible. They also need to be easily

implementable in Verilog-A using existing SPICE simulation framework. To overcome the limitations of the single pole approximation and to preserve the precision of eq. (9) as much as possible, it is crucial that one simplifies $\text{sinc}\left(\frac{\omega\tau_c}{2}\right)e^{-j\frac{\omega\tau_c}{2}}$ to a more convenient form:

$$I_{ph}(w) = I_{ph}(\omega = 0) \cdot \frac{1}{1+j\omega\tau_a} \cdot \frac{\left(e^{j\frac{\omega\tau_c}{2}} - e^{-j\frac{\omega\tau_c}{2}}\right)}{2 \cdot j \cdot \frac{\omega\tau_c}{2}} \cdot e^{-j\frac{\omega\tau_c}{2}},$$

$$\text{Or, } I_{ph}(w) = I_{ph0} \frac{1}{1+j\omega\tau_a} \cdot \frac{(1-e^{-j\omega\tau_c})}{j\omega\tau_c}. \quad (12)$$

Substituting the Laplace variable $s = j\omega$ in (12), the frequency domain representation reads,

$$I_{ph}(s) = I_{ph0} \frac{1}{1+s\tau_a} \cdot \frac{(1-e^{-s\tau_c})}{s\tau_c}. \quad (13)$$

To implement the above equation in Verilog-A, one needs to consider that the Laplace variable, s , in fact stands for the time derivative, ddt . However, implementation of second order expressions in Verilog-A is not directly possible without a few approximations to rearrange the transfer function in terms of simple single pole equivalent circuits making use of Kirchhoff's current law at each of these equivalent circuit nodes in terms of lumped R, L or C elements.

The accuracy of the approximation and the computation burden are the two factors that we kept in mind while searching for an optimal solution that offers a good balance between accuracy and computational efficiency. Before arriving at the model proposed in this work, we explored several approximation methods which included Taylor series and Padé approximants [25] particularly for approximating the exponential term in (13). These provided better accuracy compared to the classical single pole model, both in terms of magnitude and phase of the photo-response, but they were either computationally expensive or lacked the desired precision (Fig. 4). For example, a 4th order Taylor series expansion not only deviates rapidly from the analytical solution beyond 100 GHz both in magnitude and phase as shown in Fig. 4, but also requires 6 additional node for its implementation.

While the Padé approximants [25] of lower orders (Padé(1,1) or Padé(2,1)) were relatively light in terms of computational resources, requiring 2 and 3 additional nodes, respectively. Compared to the higher order Padé(3,1) approximant, which can be implemented with 5 additional nodes, the lower order approximants were also unable to capture the desired precision of the analytical equation. As shown in Fig. 4, while both the Padé(2,1) and Padé(3,1) approximants exhibit better precision over Padé(1,1) in both the magnitudes and phase, the magnitudes of Padé(2,1) and Padé(3,1) approximants start to deviate from the analytical solution beyond 100 GHz. However, the phase of the Padé(3,1) approximant shows the best fit with the analytical solution among all the methods explored so far. However, the sheer computation burden of the approximation was still not acceptable.

Hence, in this paper, we propose a new implementation making use of the Taylor series for the exponential term. We will show that this new implementation not only ensures very high model precision up to very high frequencies (up to 300 GHz) but also optimizes computational burden by limiting the polynomial expansion to its third order, thereby limiting the

number of additional nodes to 3 in Verilog-A implementation. First, eq. (13) in Laplace domain is re-written as

$$I_{pha}(s) = I_{ph}(s) \cdot \frac{s\tau_c}{(1-e^{-s\tau_c})}, \text{ with } I_{pha}(s) = I_{ph0} \frac{1}{1+s\tau_a}. \quad (14)$$

Considering that $s\tau_c/(1-e^{-s\tau_c})$ has a polynomial expansion of the form $[C_0 + C_1(s\tau_c) + C_2(s\tau_c)^2 + \dots]$ and substituting the Taylor series for $e^{s\tau_c}$, one can solve for coefficient values C_0, C_1 and C_2 . If one writes,

$$\frac{s\tau_c e^{s\tau_c}}{(e^{s\tau_c} - 1)} = C_0 + C_1(s\tau_c) + C_2(s\tau_c)^2 + \dots$$

$$\text{Or, } s\tau_c \left(1 + s\tau_c + \frac{(s\tau_c)^2}{2} + \frac{(s\tau_c)^3}{6} + \dots\right)$$

$$= (C_0 + C_1(s\tau_c) + C_2(s\tau_c)^2 + \dots) \cdot \left(s\tau_c + \frac{(s\tau_c)^2}{2} + \frac{(s\tau_c)^3}{6} + \dots\right) \quad (15)$$

Solving from both sides for the polynomial coefficients, we obtain, $C_0=1, C_1=1/2$ and $C_2=1/12$. Limiting the expansion to its 3rd order and rewriting (14) using these values, we obtain,

$$I_{pha}(s) = I_{ph}(s) \left[1 + \frac{s\tau_c}{2} + \frac{(s\tau_c)^2}{12}\right] \quad (16)$$

$$\text{or, } I_{ph}(s) = \frac{I_{pha}(s)}{[1+s\tau_c/2+(s\tau_c)^2/12]} \quad (17)$$

Eq. (17) can now be translated into Verilog-A by representing each pole using its equivalent R-C network. For this, one can write the corresponding Kirchhoff's current equations at each node in terms of the node currents and voltages. The capacitive elements are represented by the time derivatives, ddt , of the node voltages to replace the Laplace variable.

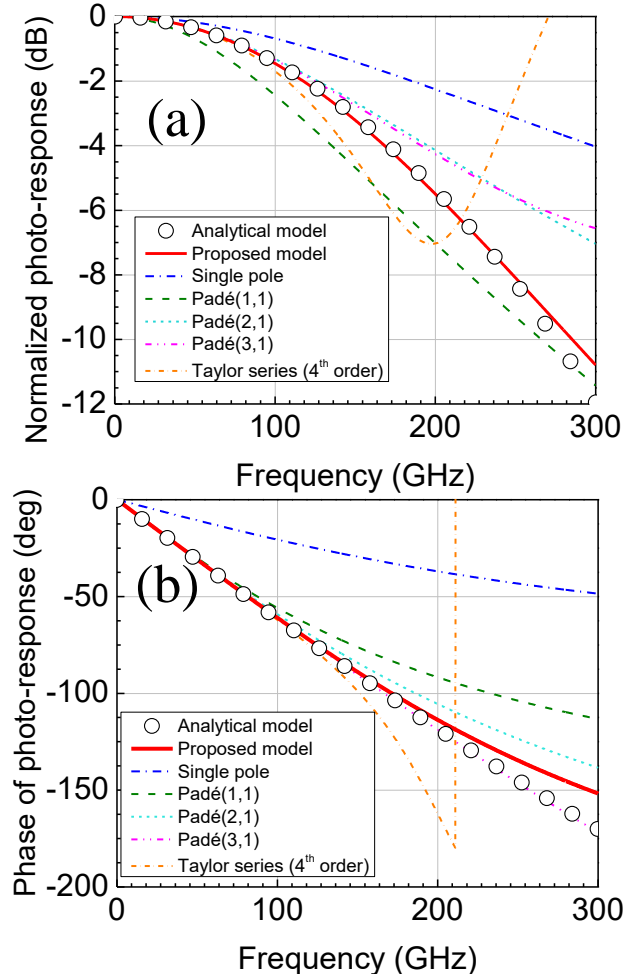


FIG. 4: Normalized photo-response comparing analytical solution with different approximations studied.

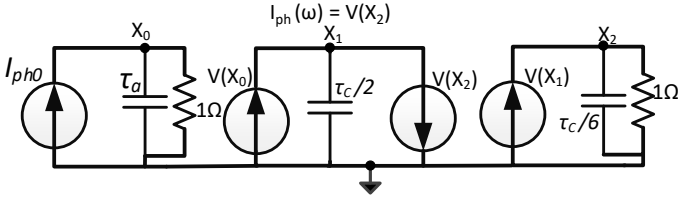


FIG. 5: Electrical equivalent circuit of the proposed implementation.

Eq. (17) was represented by three additional sub-circuits in the SPICE model (Fig. 5), similar to the approach presented in [20]. Using Kirchhoff's current law, the following equations for Verilog-A implementation can be written,

$$\left. \begin{aligned} I_{ph0} - V(X_0) - \text{ddt}(\tau_a \cdot V(X_0)) &= 0, \\ V(X_0) - V(X_2) - \text{ddt}\left(\frac{\tau_c}{2} \cdot V(X_1)\right) &= 0 \\ V(X_1) - V(X_2) - \text{ddt}\left(\frac{\tau_c}{6} \cdot V(X_2)\right) &= 0 \end{aligned} \right\} \quad (18)$$

Solving the equations in (18) simultaneously for $V(X_2)$ gives $I_{ph}(\omega)$. As pointed out in [26], it is important to note that default convergence tolerance in Verilog-A is 10^{-6} for node voltages and 10^{-12} for currents, typically. Due to this reason, the assignment of a current to a node voltage while solving for model-intrinsic node variables, as is the case for (18), results in the convergence tolerances mismatched by a factor of 10^6 that might lead to simulation problems. Particularly, in circuit simulation scenarios, if the values stored in internal node voltages unexpectedly and significantly differ from typical voltage values, problems in transient simulation might be encountered due to the simulation convergence criteria. Hence, in accordance with the best practices of Verilog-A compact modeling [26], the current I_{ph0} is scaled by a factor of 10^6 so that defined tolerances for voltage quantities are not exceeded. Finally, the solution obtained for $V(X_2)$ is again scaled by 10^{-6} to obtain the correct value of the photocurrent:

$$\left. \begin{aligned} 10^6 * I_{ph0} - V(X_0) - \text{ddt}(\tau_a \cdot V(X_0)) &= 0, \\ V(X_0) - V(X_2) - \text{ddt}\left(\frac{\tau_c}{2} \cdot V(X_1)\right) &= 0 \\ V(X_1) - V(X_2) - \text{ddt}\left(\frac{\tau_c}{6} \cdot V(X_2)\right) &= 0 \\ I_{ph} &= 10^{-6} * V(X_2) \end{aligned} \right\} \quad (19)$$

This new implementation shows very good model accuracy over the entire frequency range up to 300 GHz compared to the analytical solution (Fig. 4), both for the magnitude and the phase, offering the best compromise between computational effort and precision. In Fig. 6, 3-dB cut-off frequencies of different UTC-PD technologies from III-V lab [3], ETH Zurich [7], IEMN [27] and UCL [8] were calculated using the analytical expression of photocurrent for various absorber and collector widths, affirming the versatility and applicability of our proposed model with respect to the most commonly reported UTC-PD structures. In Fig. 7, the RMS errors in the magnitude and the phase with respect to (9), obtained using the same physical parameters in table 1, are shown for three implementations. For this comparison, we chose the Padé (1,1) and Padé (3,1) implementations since they are computationally the least and most exhaustive, respectively. Contrastingly, our proposed model, which offers the highest precision in both magnitude and phase, requires an optimal

implementation effort, offering the best trade-off between model accuracy and computation. Considering the absorber and collector thicknesses corresponding to their highest 3-dB cut-off frequencies (Fig. 6), we note the lowest RMS error (1-6% in magnitude and 0.5-1.5% in phase) for our proposed implementation (Figs. 7(e) and (f)) compared to the others (Figs. 7 (a), (b) and (c), (d)). To the best of our knowledge, our proposed implementation is the first demonstration of such accurate SPICE model of photocurrent in UTC-PDs.

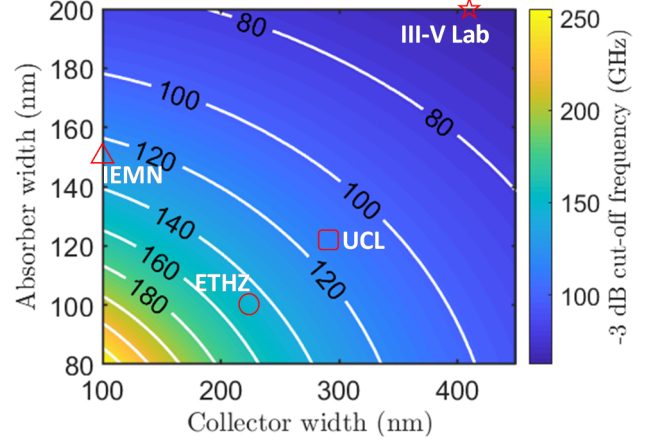


FIG. 6: 3-dB cut-off frequencies of various UTC-PD technologies [3, 7-8, 25].

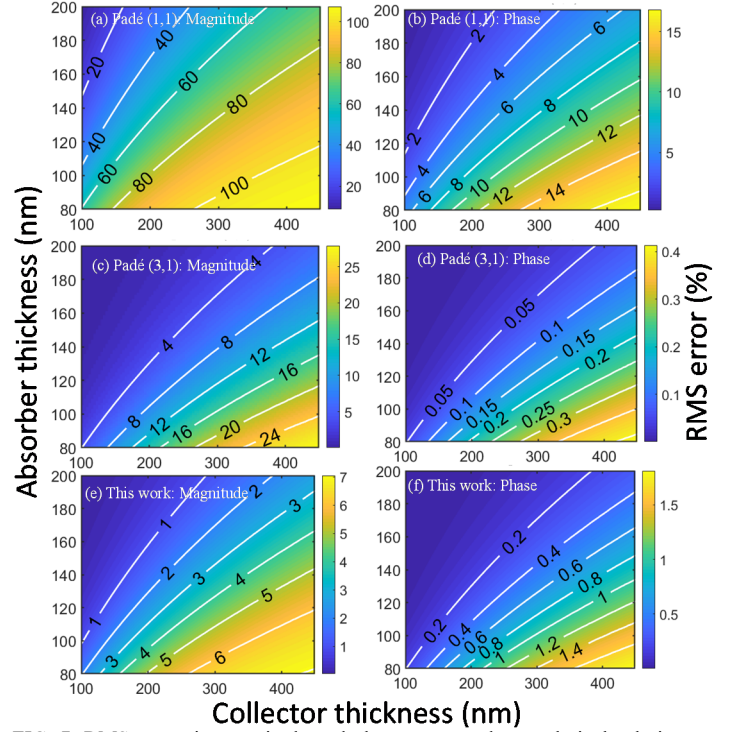


FIG. 7: RMS errors in magnitude and phase compared to analytical solution for (a) and (b) Padé (1, 1); (c) and (d) Padé (3, 1); (e) and (f) our proposed approximation methods.

IV. MODEL VALIDATION

The theoretical expression of the photo-current transfer function in (9) is in fact the intrinsic photo-carrier response of the photodiodes. However, one must keep in mind that on-wafer measurement results also include the transfer functions due to the R-C delay of the diode junction capacitance and series resistance and that of the RF test-structures. Therefore, the measured results show a lower than predicted (by eq. (9))

3-dB cut-off frequency. To take this into account for model validation, we leveraged the UTC-PD SPICE compact model and associated parameter set without illumination (detailed in [14-15]) for the simulation of dynamic photo-response. Results are shown in Figs. 8 (a) and (b) for InGaAs/InGaAsP [3] and GaInAsSb/InP [7] UTC-PDs, respectively, comparing on-wafer measurements with compact model simulations for different approximation methods. Corresponding simulation results for the single pole approximation are also included for reference. As expected, the single pole approximation overestimates the cut-off frequency, whereas Padé (1, 1) approximation underestimates it. Interestingly, both Padé (2, 1) and Padé (3, 1) show quite acceptable precision up to 67 GHz and start to deviate from the analytical solution beyond 110 GHz (Fig. 8). Our proposed implementation offers the best trade-off between accuracy and computational efficiency for implementation of the photo-response, remaining accurate even beyond 110 GHz. Due to equipment limitation of on-wafer measurements, precision of different implementations could not be further evaluated experimentally at very high frequencies. However, for integrated photonic circuit design employing high-bandwidth photodiodes such as the ones reported in [15, 16], the accuracy and computational efficiency of our proposed model at such high frequencies will be indispensable. Availability of on-wafer measurements beyond 110 GHz will therefore offer a stronger validation of our proposed photo-response SPICE modeling framework.

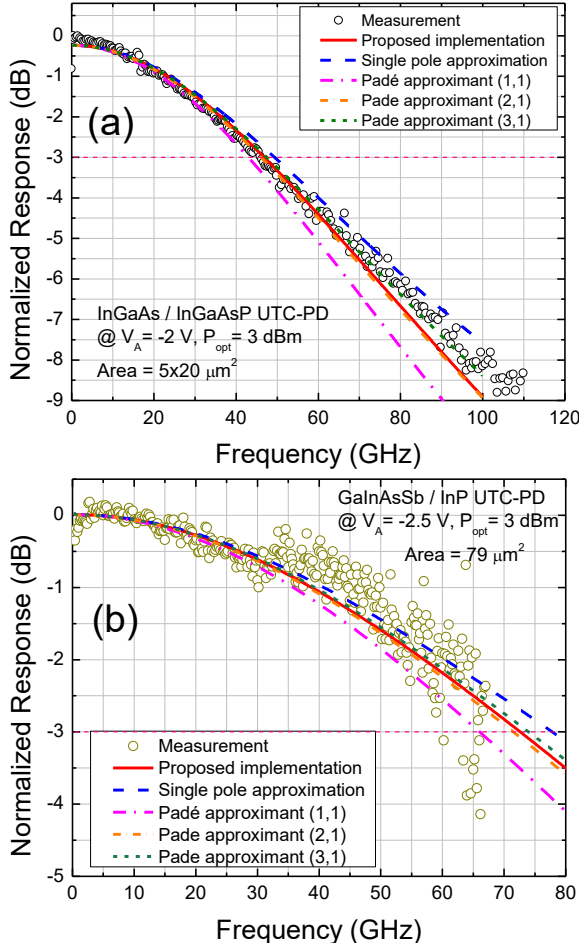


FIG. 8: Measured (symbol) and simulated (line) normalized photo-response of (a) InGaAs/InGaAsP and (b) GaInAsSb/InP UTC-PDs comparing different photocurrent implementations methods investigated in this work.

V. CONCLUSION

In this paper we reported the first accurate and physics-based Verilog-A SPICE compact model implementation of the complete analytic form of the photocurrent in UTC-PDs. Our proposed implementation makes use of an optimal number of 3 additional nodes in the UTC-PD electrical equivalent circuit offering the best compromise between precision and computational efficiency. Model simulation has been validated against on-wafer measurements of two UTC-PD technologies, depicting very good accuracy up to 67 and 110 GHz. In future, we plan on further exploring experimental validation, especially for the phase of the photo-response, using additional optical characterization techniques and leveraging high-frequency measurements. From a theoretical point of view, our proposed implementation preserves model accuracy up to 300 GHz compared to other approximation methods, thereby making it indispensable for future high-speed OEIC design.

APPENDIX

Verilog-A code for the proposed implementation of the UTC photocurrent model:

```

module photodiode (Anode, Cathode, Light) ;
inout Anode, Cathode, Light;
electrical Anode, Cathode, Light;
// Virtual nodes for photocurrent implementation
electrical x1, x2, x3;
// Current branches
// UTC-PD CURRENTS
branch (Anode, Cathode) PD_branch ;
// Light port
branch (Light) br_light ;

// Virtual branches
branch (x1) br_bx1;
branch (x2) br_bx2;
branch (x3) br_bx3;
...
`define MPRcz (nam, def, uni, des) \
(*units=uni, desc=des*) \
parameter real nam=def from[0:inf];
// Model parameters
MPRcz (Responsivity, 0.5, "A/W", "Responsivity")
MPRcz (WA, 100e-9, "m", "Absorber thickness")
MPRcz (WC, 225e-9, "m", "Collector thickness")
MPRcz (mu, 0.5, "m^2/Vs", "e mobility")
MPRcz (vth, 2.5e5, "m/s", "thermionic emiss. vel.")
MPRcz (vsat, 1e5, "m/s", "saturation velocity") ...
real Iph, Popt, De, Id, I5;
real tauA, tauC;

analog begin
// PHOTO-CURRENT CALCULATION
De=mu*0.026;
tauA=WA*WA/(3*De)+WA/vth;
tauC=WC/vsat;
...
// dB to Watt conversion for input optical power
Popt = pow(10, 0.1*V(br_light))/1000;
Iph=Popt*Responsivity;
...
// Single pole calculations
I(br_bx1)<+=Iph;
I(br_bx1)<+=V(br_bx1);
I(br_bx1)<+=ddt(tauA*V(br_bx1));

// Implementation of sinc(w*tauA)*exp(-jw*tauC)
I(br_bx2)<+=-V(br_bx1)+V(br_bx3);
I(br_bx2)<+=ddt((tauC/2)*V(br_bx2));

```

```

I(br_bx3)<+-V(br_bx2);
I(br_bx3)<+V(br_bx3);
I(br_bx3)<+ddt((tauC/6)*V(br_bx3));
...

// Total diode current
Id=diode current equations;

// Photocurrent branch
I5=V(br_bx3);

// CURRENT CONTRIBUTION
...
I(PD_branch)<+Id; //Diode current
I(PD_branch)<+-I5; //Photocurrent
end
endmodule

```

REFERENCES

- [1] C. R. Doerr, L. Zhang, P. J. Winzer, N. Weimann, V. Houtsma, T.-C. Hu, N. J. Sauer, L. L. Buhl, D. T. Neilson, S. Chandrasekhar, and Y. K. Chen, "Monolithic InP Dual-Polarization and Dual-Quadrature Coherent Receiver," in *IEEE Photonics Technology Letters*, vol. **23**, no. 11, pp. 694-696, June 1, 2011, DOI: [10.1109/LPT.2011.2123088](https://doi.org/10.1109/LPT.2011.2123088).
- [2] D. Konstantinou, C. Caillaud, T. Shivan, S. Rommel, U. Johannsen, F. Blache, F. Mallecot, V. Krozer, and I. T. Monroy, "Simulation of an Integrated UTC-Photodiode with a High-Speed TIA for 5G mm-Wave Generation," 2020 International Conference on Numerical Simulation of Optoelectronic Devices (NUSOD), 2020, pp. 1-2, DOI: [10.1109/NUSOD49422.2020.9217642](https://doi.org/10.1109/NUSOD49422.2020.9217642).
- [3] C. Caillaud, H. Bertin, A. Bobin, R. Gnanamani, N. Vaissiere, F. Pommereau, J. Decobert and C. Maneux, "Ultra Compact High responsivity Photodiodes for >100 Gbaud Applications," *2021 European Conference on Optical Communication (ECOC)*, 2021, pp. 1-4, doi: [10.1109/ECOC52684.2021.9606076](https://doi.org/10.1109/ECOC52684.2021.9606076).
- [4] N. Weimann, "InP HBT technology for THz applications," 2020 IEEE International Symposium on Radio-Frequency Integration Technology (RFIT), 2020, pp. 190-192, DOI: [10.1109/RFIT49453.2020.9226243](https://doi.org/10.1109/RFIT49453.2020.9226243).
- [5] M. Natrella, C.-P. Liu, C. Graham, F. van Dijk, H. Liu, C. C. Renaud and A. J. Seeds, "Accurate equivalent circuit model for millimetre-wave UTC photodiodes", *Opt. Express*. Vol. **24**, pp. 4698-4713, 2016. DOI: [10.1364/OE.24.004698](https://doi.org/10.1364/OE.24.004698)
- [6] Q. Q. Meng, H. Wang, B. Gao, C. Y. Liu, K. S. Ang, X. Guo, and J. Gao, "Equivalent Circuit Model for InP-based Uni-Traveling-Carrier Photodiodes with Dipole-doped Structure," in *Asia Communications and Photonics Conference 2014*, OSA Technical Digest (online) (Optica Publishing Group, 2014), paper ATH3A.22. DOI: [10.1364/ACPC.2014.ATH3A.22](https://doi.org/10.1364/ACPC.2014.ATH3A.22)
- [7] A. Arabhavi, R. Chaudhary, R. Fluckiger, D. Marti, S. Hamzeloui, F. Ciabattini, W. Quan, M. Leich, O. Ostinelli, and C. R. Bolognesi, "Type-II GaInAsSb/InP Uniform Absorber High Speed Uni-Traveling Carrier Photodiodes", *J. Lightwave Technol* vol. **39**, 2171-2176, 2021. DOI: [10.1109/JLT.2020.3043537](https://doi.org/10.1109/JLT.2020.3043537)
- [8] M. Natrella, C.-P. Liu, C. Graham, F. van Dijk, H. Liu, C. C. Renaud, and A. J. Seeds, "Modelling and measurement of the absolute level of power radiated by antenna integrated THz UTC photodiodes," *Opt. Express* vol. 24, pp. 11793-11807, 2016. DOI: [10.1364/OE.24.011793](https://doi.org/10.1364/OE.24.011793)
- [9] H.F. Wen, Q. H. Nie, T. F. Xu, T. J. Liu, X. Y. Ying, K. Clark, Y. F. Li, "High Accuracy Modeling Method of UTC-PD Photodiode" *Advanced Materials Research*, Vols. **712-715**, pp 1775-1779, 2013. <https://doi.org/10.4028/www.scientific.net/amr.712-715.1775>.
- [10] T. Ishibashi, S. Kodama, N. Shimizu and T. Furuta, "High-Speed Response of Uni-Traveling-Carrier Photodiodes" *Jpn. J. Appl. Phys.* Vol. 36, pp. 6263, 1997. DOI: [10.1143/JJAP.36.6263](https://doi.org/10.1143/JJAP.36.6263)
- [11] T. Ishibashi and H. Ito, "Uni-traveling-carrier photodiodes". *J. Appl. Phys.* vol. 127, pp. 031101, 2020. DOI: [10.1063/1.5128444](https://doi.org/10.1063/1.5128444)
- [12] T. Ishibashi, T. Furuta, H. Fushimi, S. Kodama, H. Ito, T. Nagatsuma, N. Shimizu and Y. Miyamoto, "InP/InGaAs Uni-Traveling-Carrier Photodiodes," *IEICE Trans. Electron.*, vol. E83-C, no. 6, 2000.
- [13] C. Mukherjee, M. Natrella, J. Seddon, C. Graham, P. Mounaix, C. C. Renaud and C. Maneux, "Efficient compact modelling of UTC-photodiode towards terahertz communication system design", *Solid State Electron.* Vol. **170**, pp. 107836, May 2020. DOI: [10.1016/j.sse.2020.107836](https://doi.org/10.1016/j.sse.2020.107836)
- [14] C. Mukherjee, M. Deng, V. Nodjiadjim, M. Riet, C. Mismer, D. Guendouz, C. Caillaud, H. Bertin, N. Vaissiere, M. Luisier, X. Wen, M. De Matos, P. Mounaix, and C. Maneux, "Towards Monolithic Indium Phosphide (InP)-Based Electronic Photonic Technologies for beyond 5G Communication Systems," *Appl. Sci.*, vol. **11**, no. 5, p. 2393, Mar. 2021. DOI: [10.3390/app11052393](https://doi.org/10.3390/app11052393)
- [15] D. Guendouz, C. Mukherjee, M. Deng, M. De Matos, C. Caillaud, H. Bertin, A. Bobin, N. Vaissiere, K. Mekhazni, F. Mallecot, A. K. Arabhavi, R. Chaudhary, O. Ostinelli, C. Bolognesi, P. Mounaix, and C. Maneux, "Multiscale Compact Modelling of UTC-Photodiodes Enabling Monolithic Terahertz Communication Systems Design," *Applied Sciences*, vol. **11**, no. 23, p. 11088, Nov. 2021, DOI: [10.3390/app112311088](https://doi.org/10.3390/app112311088).
- [16] S. Lischke, A. Peczek, J. S. Morgan, K. Sun, D. Steckler, Y. Yamamoto, F. Korndörfer, C. Mai, S. Marschmeyer, M. Fraschke, A. Krüger, A. Beling and L. Zimmermann, "Ultra-fast germanium photodiode with 3-dB bandwidth of 265 GHz", *Nat. Photon.* Vol. **15**, pp. 925-931, 2021. DOI: [10.1038/s41566-021-00893-w](https://doi.org/10.1038/s41566-021-00893-w)
- [17] E. Rouvalis, M. Chtioui, F. van Dijk, F. Lelarge, M. J. Fice, C. C. Renaud, G. Carpintero, and A. J. Seeds, "170 GHz uni-traveling carrier photodiodes for InP-based photonic integrated circuits," *Opt. Express* vol. **20**, pp. 20090-20095, 2012. DOI: [10.1364/OE.20.020090](https://doi.org/10.1364/OE.20.020090)
- [18] F. Pavanello, "Uni-traveling carrier photodiodes and metal mesh filters based on sub-wavelength apertures for THz applications", Thesis, University of Science and Technology, Lille, 2013.
- [19] ATLAS User's Manual, Silvaco International, Santa Clara, 2004 www.silvaco.com.
- [20] T. Ishibashi and H. Ito, "Uni-Traveling Carrier Photodiodes: Development and Prospects," *IEEE Journal of Selected Topics in Quantum Electronics*, vol. 28, no. 2: Optical Detectors, pp. 1-6, March-April 2022, no. 3803006, doi: [10.1109/JSTQE.2021.3123383](https://doi.org/10.1109/JSTQE.2021.3123383).
- [21] P.-L. Liu, K. J. Williams, M. Y. Frankel and R. D. Esman, "Saturation characteristics of fast photodetectors," *IEEE Transactions on Microwave Theory and Techniques*, vol. 47, no. 7, pp. 1297-1303, July 1999, doi: [10.1109/22.775469](https://doi.org/10.1109/22.775469).
- [22] Y. Fu, H. Pan, Z. Li, A. Beling and J. C. Campbell, "Characterizing and Modeling Nonlinear Intermodulation Distortions in Modified Uni-Traveling Carrier Photodiodes," *IEEE Journal of Quantum Electronics*, vol. 47, no. 10, pp. 1312-1319, Oct. 2011, doi: [10.1109/JQE.2011.2165700](https://doi.org/10.1109/JQE.2011.2165700).
- [23] W. Zhang, T. Li, M. Lours, et al. "Amplitude to phase conversion of InGaAs pin photo-diodes for femtosecond lasers microwave signal generation" *Appl. Phys. B* **106**, 301-308 (2012). doi: [10.1007/s00340-011-4710-1](https://doi.org/10.1007/s00340-011-4710-1)
- [24] E. N. Ivanov, S. A. Diddams and L. Hollberg, "Study of the excess noise associated with demodulation of ultra-short infrared pulses," *IEEE Transactions on Ultrasonics, Ferroelectrics, and Frequency Control*, vol. 52, no. 7, pp. 1068-1074, July 2005, doi: [10.1109/TUFFC.2005.1503992](https://doi.org/10.1109/TUFFC.2005.1503992)
- [25] H. Padé, « Sur la représentation approchée d'une fonction par des fractions rationnelles ». *Annales scientifiques de l'École Normale Supérieure*, vol. **9**, no. 3, pp. 3-93, 1892. DOI : [10.24033/asens.378](https://doi.org/10.24033/asens.378)
- [26] C. C. McAndrew, Z. Huszka and G. J. Coram, "Bipolar Transistor Excess Phase Modeling in Verilog-A," in *IEEE Journal of Solid-State Circuits*, vol. 44, no. 9, pp. 2267-2275, Sept. 2009, doi: [10.1109/JSSC.2009.2022667](https://doi.org/10.1109/JSSC.2009.2022667).
- [27] P. Latzel, F. Pavanello, M. Billet, S. Bretin, A. Beck, M. Vanwolleghem, C. Coinon, X. Wallart, E. Peytavit, G. Ducournau, M. Zaknounge, and J.-F. Lampin, "Generation of mW Level in the 300-GHz Band Using Resonant-Cavity-Enhanced Unitraveling Carrier Photodiodes," *IEEE Trans. Terahertz Sci. Technol.* vol. **7**, no. 6, pp. 800-807, Nov. 2017. DOI: [10.1109/TTHZ.2017.2756059](https://doi.org/10.1109/TTHZ.2017.2756059)